JGR Oceans

RESEARCH ARTICLE
10.1029/2019JC015833

A Synthesis of Observations and Models to Assess the Time Series of Sea Ice Mass Balance in the Beaufort Sea

Cameron J. Planck[1], Donald K. Perovich[1], and Bonnie Light[2]

[1]Thayer School of Engineering, Dartmouth College, Dartmouth, NH, USA, [2]Polar Science Center, Applied Physics Laboratory, University of Washington, Seattle, WA, USA

Key Points:
- Eight Lagrangian mass balance sites that drifted in the Beaufort Sea from 1997–2015 showed a net loss of ice between 29–271 cm
- Bottom melting ranged from 43–220 cm and was the leading cause of ice loss at seven of the eight sites after the year 2000
- A linear relationship between solar heat deposited into the ocean and the heat used in bottom melting was found

Correspondence to:
C. J. Planck,
cameron.j.planck.th@dartmouth.edu

Citation:
Planck, C. J., Perovich, D. K., & Light, B. (2020). A synthesis of observations and models to assess the time series of sea ice mass balance in the Beaufort Sea. *Journal of Geophysical Research: Oceans*, *125*, e2019JC015833. https://doi.org/10.1029/2019JC015833

Received 30 OCT 2019
Accepted 11 OCT 2020
Accepted article online 15 OCT 2020

Abstract Over the past four decades, there has been a substantial thinning of the summer sea ice cover in the Beaufort Sea. Variations in sea ice mass balance reflect these changes and give insight to the environmental forcings which caused them. In this work, the time series results from eight Lagrangian mass balance sites that operated in the Beaufort Sea over the years 1997–2015 are analyzed. Direct measurements from the sites are combined with estimates of ice/ocean heat input to examine the roll of solar heating on ice loss, growth, and melt rates. Comparisons between ice and snow conditions and mass balance event timing, for example, surface and bottom melt onset, melt peak, and melt end, are also made. From the late 1990s to the present, a general increase in bottom melting and solar heat input to the upper ocean was observed. All sites showed a net loss of ice (ranging from 29 to 271 cm), and all but one site saw the majority of this loss from bottom melting. Bottom melt onset occurred within a relatively narrow 13-day window between 1 and 13 June at all sites. The amount of observed bottom melt was also related to the heat deposited in the ocean available for melting, underscoring the increasingly important role of ocean thermodynamics in determining sea ice mass balance.

Plain Language Summary Sea ice mass balance is a simple, yet important, parameter. It is simply the difference between ice grown in the winter and ice melted in the summer. In this study, the yearly time series from eight sea ice mass balance sites that drifted from 1997–2015 in the Beaufort Sea are studied. All but one of the sites operated for a full year through the melt season. From the data, total amounts of ice growth and melt, snow accumulation, onset and ending dates, and melt rates were determined. Comparisons between observations and estimates of solar heat input from models and ice concentrations from satellites were then made. At all sites, more ice was melted than was grown, and at seven of the eight sites, the main source of this loss was bottom melting. The onset of bottom melting also occurred during a narrow 13-day window at all sites. Lastly, the total amount of bottom melt was correlated to the amount of solar heat absorbed in the ocean.

1. Introduction

One of the most profound manifestations of global climate change is the rapidly shrinking Arctic sea ice cover. Since the beginning of the satellite record, summer ice extent has shown a consistently negative trend that has worsened since the mid-2000s (Serreze & Meier, 2019; Stroeve et al., 2012). Average ice age has decreased, and there has been a general transition from thick multiyear ice to thinner first year ice (Comiso, 2012; King et al., 2017; Kwok et al., 2009; Kwok & Rothrock, 2009; Maslanik et al., 2011). While change is occurring all across the Arctic, some of the greatest changes have been observed in the Beaufort Sea (Perovich & Richter-Menge, 2015). Historically, the Beaufort Sea has been regarded as a growth area for multiyear ice, thickening it through entrapment by the anticyclonic, wind-driven current known as the Beaufort Gyre (Thorndike & Colony, 1982). However, the Beaufort Sea has been a location of some of the largest multiyear ice losses in recent years, indicating that this may no longer be the case (Krishfield et al., 2014; Kwok & Cunningham, 2010). Reductions in multiyear ice concentration have created an ice pack that is younger, weaker, more mobile, slower to freeze up, and overall less resilient to anomalous forcing (Holland et al., 2006; Lei et al., 2018; Petty et al., 2016).

The changes occurring in the Beaufort have been linked to a variety of interconnected processes, including increasing Arctic-wide surface air temperature (Serreze et al., 2009), a lengthening melt season (Stroeve et al., 2014; Wang et al., 2013), cloud influence on incident shortwave and longwave fluxes

(Kay & Gettelman, 2009), ice preconditioning (Hutchings & Perovich, 2015; Lindsay et al., 2009), and increased solar heat deposition through ice-albedo feedback (Perovich et al., 2008). Other work has attributed decreases in Beaufort minimum ice extent to changing atmospheric circulation patterns, poleward winds and ice drift, and an increasing role of thermodynamics (Hutchings & Rigor, 2012; Overland & Wang, 2005). While interannual and spatial variability in sea ice melt remains large across the Arctic, the Beaufort has also stood out as a location with above average ice loss from bottom melting (Perovich & Richter-Menge, 2015; Perovich et al., 2008).

Forecasting the future state of the Beaufort sea ice cover requires the ability to connect changes in the ice cover to environmental forcings that are complicated and generally not well understood (Carmack & Melling, 2011). One method of simplifying this problem is through the study of sea ice mass balance, which, in the simplest terms, can be thought of as the difference between ice grown in the winter and ice melted in the summer. Because sea ice exists at the boundary of ocean and atmosphere, its mass is largely controlled by heat fluxes at these interfaces (Lei et al., 2018). If there is a net cooling over time, the ice will grow, and if there is a net warming over time, the ice will thin. This feature makes mass balance a powerful tool for understanding the net effect of the many parallel heat transfer processes occurring on the ice at a given time.

Across the Arctic, mass balance measurements have been made regularly during field campaigns since the 1960s (Perovich, 2003; Untersteiner, 1961). They have also been enabled through development and deployment of autonomous instruments, such as Ice Mass Balance buoys (IMBs) and Seasonal Ice Mass Balance buoys (SIMBs) (Jackson et al., 2013; Planck et al., 2019; Polashenski et al., 2011; Richter-Menge et al., 2006). Since 1993, IMBs and SIMBs have been deployed during many observational campaigns, including the North Pole Environmental Observatory (NPEO), the Arctic Observing Network (AON), and the Beaufort Gyre Exploration Project (BGEP). The main advantage to (S)IMBs is that they permit year-round monitoring of sea ice mass balance without the large resources and expense required to maintain field camps. IMBs and SIMBs also independently measure ice surface and bottom position, allowing thickness changes to be attributed to atmospheric and oceanic forcing (Perovich, Richter-Menge et al., 2011; Perovich et al., 2008, 2014). (S)IMB results thus provide an excellent starting point for investigating the integrated effect of a changing climate on the mass of the sea ice cover.

Improving understanding of the connection between observed changes to the Beaufort sea ice cover and the driving forces which caused them is the motivation of this study. More specifically, the goals of this work are summarized by three high level questions: (i) How has the seasonal evolution of sea ice mass balance in the Beaufort Sea changed over the 1997–2015 period? (ii) Over this time span, what parameters influenced ice growth or melt? And lastly, (iii) how is summer melt partitioned between atmospheric and oceanic driven processes? The pursuit of question (i) began by tabulating the results from eight Lagrangian mass balance sites that drifted in the Beaufort Sea over the 1997–2015 time span. From these data, the time series of snow accumulation, ice growth, and surface and bottom ablation were determined. The onset and ending dates of surface and bottom growth and melt were classified, as were the weekly growth and melt rates. Growth and melt magnitudes, rates, and timings were then compared across sites and across years. For questions (ii) and (iii), estimates of solar heat deposition to the ice and ocean were computed along the drift track for each site using incident shortwave solar estimates from the Modern-Era Retrospective Analysis for Research and Applications (MERRA) reanalysis product, satellite-derived ice concentrations, and PIOMAS model outputs. The amount of solar heat deposited into the ice cover at each site was determined, as was the amount entering the upper ocean through ice transmission and lead absorption. Statistical relationships between observed quantities, such as initial ice thickness, snow accumulation, and net ice loss, were then calculated and compared with the goal of discovering potential mass balance proxies. Finally, the cumulative solar heat deposited into the ice and ocean nearest the site location on 15 August was compared to the heat used in surface and bottom melting.

2. Instruments, Methods, and Data Sets

Seven of the eight data sets analyzed were obtained from autonomous IMBs, which collect time series of sea ice mass balance by directly measuring changes in ice surface and bottom position from an in situ, ice-fixed position. The eighth data set was taken during the Surface Heat Budget of the Arctic (SHEBA) drifting

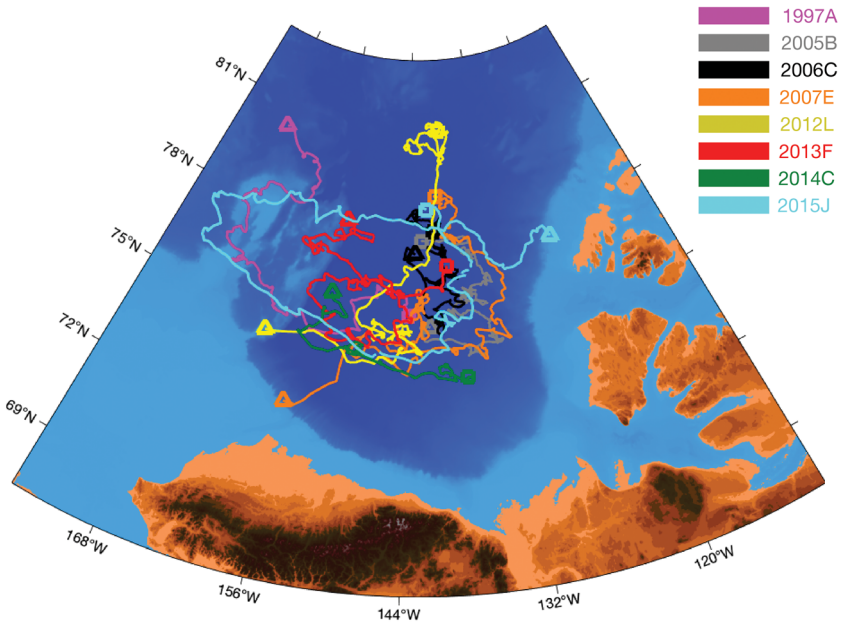

Figure 1. Drift tracks of the eight ice mass balance sites. The starting and ending points are denoted by a square and a triangle, respectively, and the sites are color coded in all figures according to the legend. The map background indicates water depth, where darker blue is deeper water. Note that while starting points varied, many of the sites overlapped considerably along their trajectories.

campaign from 1997–98 and was made using a combination of automated and manual measurements (Perovich, 2003; Perovich & Elder, 2002). Drift tracks from each of these sites are given in Figure 1.

2.1. IMBs

At a high level, an IMB is simply an automated thickness gauge and ablation stake. Their primary function is to translate with the floe and measure a one-dimensional time series of ice growth, snow accumulation, and surface and bottom melt. In this paper, analysis was restricted to data sets from IMBs and SIMBs as defined by Richter-Menge et al. (2006) and Polashenski et al. (2011), respectively. These instruments are unique in that they directly measure ice (or snow) surface and bottom position using a pair of acoustic rangefinders positioned above and below the ice (Figures 2a and 2b). By using acoustic rangefinders, the instruments are able to determine surface and bottom position changes without reliance on vertical temperature profile. This feature aids in the measurement of surface and bottom melt during the summer months when the ice becomes vertically isothermal.

2.1.1. Standard IMB

Figure 2a gives the schematic of a standard IMB, which was designed for measurement in thick ice that does not fully melt out every year (multiyear ice). These instruments were initially developed in 1993 at the Cold Regions Research and Engineering Laboratory (CRREL) in Hanover, New Hampshire, but have since been transferred to MetOcean in Dartmouth, Nova Scotia, Canada (https://www.metocean.com), for production. The IMB instrument package consists of a pair of ice-facing acoustic rangefinders (±0.01-m resolution), a 10-cm spaced vertical temperature string (±0.1°C resolution), air temperature and pressure sensors (±0.5°C, ±0.01-mbar resolution, respectively), and a GPS (3-m resolution), all of which are connected to a centrally located data logger and power supply. The ice-facing rangefinders are fixed to a pole of known length that is frozen into the ice during deployment. Mass balance (or rather, combined snow + ice thickness) is determined by subtracting the rangefinder distance measurements from the pole length. By combining initial measurements of snow depth and ice thickness taken during deployment, ice surface position and snow accumulation can be resolved from each other. IMB data transmission is achieved through the Iridium satellite network, and the transmission interval was typically 1 hr for latitude, longitude, air temperature, and barometric pressure and 4 hr for ice surface and bottom position

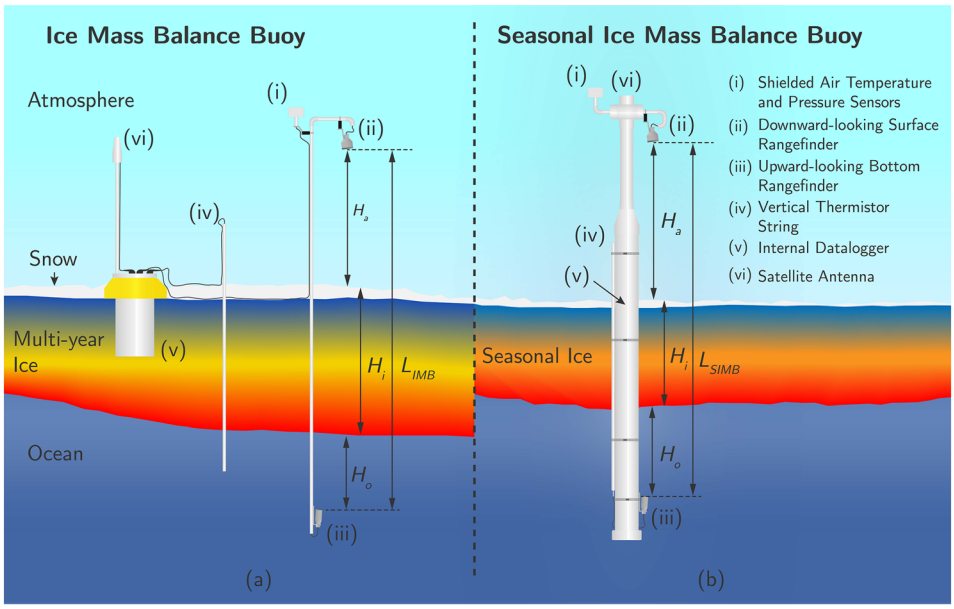

Figure 2. (a) Ice mass balance buoy (IMB) schematic. Core components are labeled with numerals and listed on the right. Note that the IMB was designed to measure thick, multiyear ice that does not fully melt out. The device is nonbuoyant and fully reliant on the ice for mechanical support. (b) Seasonal ice mass balance buoy (SIMB) schematic. The seasonal ice mass balance buoy uses mostly the same sensor suite as the IMB but is encapsulated in a floating, positively buoyant, sealed hull. The buoyant nature of the SIMB makes it operable in open water, giving the potential to measure mass balance later into the melt season than the IMB. Once frozen into the floe, the (S)IMBs acoustic rangefinders measure the distances from the rangefinder mounting points to the ice/snow surface (top) and ice bottom; H_a and H_o, respectively. The distance between the two rangefinders, LIMB and LSIMB, is also known. The total ice + snow thickness, H_i, is then calculated simply as $H_i = L(S)IMB - H_a - H_o$. With knowledge of the initial snow thickness, the snow accumulation and melt at the site can also be resolved.

and vertical temperature profile. Of the instruments presented in this manuscript, 2005B, 2006C, and 2007E were IMBs. Note that the IMB is a nonfloating design that rests directly on the ice.

2.1.2. The SIMB

Figure 2b is a SIMB. The SIMB consists of the same instrument package as the IMB but is enclosed in a hermetically sealed hull that is positively buoyant and upright floating. SIMBs are designed for operation in thin, seasonal, ice that breaks up or fully melts out each year. Being positively buoyant and upright stable, SIMBs do not rely on the ice for mechanical support and are also capable of operation in open water. Mass balance sites 2012L, 2013F, 2014C, and 2015J were SIMBs.

2.2. Site Selection Criteria

The seven IMB data sets were chosen based on their location in the Beaufort Sea, operation through the growth and melt seasons (ideally September through the following August), and data quality. A "quality" data set was defined by the presence of surface (snow or ice) and bottom (ice) measurements from the acoustic rangefinders, vertical temperature profiles, air temperature and barometric pressure measurements, and GPS locations for the duration of instruments operation. In particular, the surface and bottom rangefinder measurements are necessary to render a complete time series of sea ice mass balance, which is the focus of this article.

2.3. Interpreting (S)IMB Results

One limitation of (S)IMBs is that they collect only one-dimensional point measurements of mass balance. This fact complicates the extrapolation of IMB results to larger spatial scales where local ice/snow morphology and feedbacks govern melt and growth. Variations in sea ice mass balance are known to be significant on a pan-Arctic scale and also vary significantly across years (Perovich & Richter-Menge, 2015). The 2013 results from ice stations in the Lincoln sea observed spatial variations of ice thickness to range

from 14–24 m for multiyear ice and around 30 m for first year ice, demonstrating that regional variation is also high (Lange et al., 2017). Snow patch heterogeneity during this time also varied from 9–25 m for multiyear ice and 30–45 m for first year ice (Lange et al., 2017). While these results indicate a limitation of IMBs to assess regional variations in ice thickness and snow accumulation, relative values of melt might scale more broadly. In particular, data from the SHEBA cruise indicate that IMB results can be representative of the greater area so long as the instruments are deployed in undeformed, unponded, multiyear ice that is similar to other floes in the region (Perovich & Richter-Menge, 2006). Results from second year ice in the Transpolar Drift in November of 2007 also show good agreement between IMB-derived ice ablation and collocated electromagnetic induction sounder (EM) transects (Haas et al., 2011). Typically, when (S)IMBs are deployed, significant care is taken to ensure they are placed in ice that is not only representative of the greater area but also free of obvious signs of ice dynamics (e.g., ridges and leads). It is also important to note that, for the purpose of this article, the term "sea ice mass balance" refers strictly to thermodynamic mass balance, in other words, changes in sea ice thickness due to oceanic or atmospheric heat fluxes, not including the direct effect of dynamics.

2.4. Mass Balance Determination From (S)IMB Measurements

The rangefinder measurements (Figure 2, H_a and H_o) were taken directly from the (S)IMB data files. After buoy installation, reductions in the value of H_a were interpreted as snow accumulation. Correspondingly, increases in H_a during the melt season were interpreted as snow melt until H_a reached the initial deployment value plus the initial snow depth, indicating that all of the snow had melted and bare ice was exposed. Continued increases in H_a were then interpreted as ice surface melting. Bottom growth and melt was easier to interpret, as changes in H_o simply reflect changes in ice thickness. The onset and ending dates of snow accumulation, ice growth, and snow and ice melt were determined through inspection by the authors using H_a and H_o, their derivatives, and site air temperatures. Average values of weekly ice thickness, ice growth, surface ablation, and bottom ablation were also pulled directly from the (S)IMB measurements.

2.5. Estimating Solar Heat Deposition to Ice and Ocean Along Site Drift Track

Downwelling shortwave solar radiation (F_r) was estimated on a daily basis using the MERRA reanalysis product (Rienecker et al., 2011). Ice concentration (C) was determined using the NSIDC Passive Microwave Satellite Ice Concentration data set (Cavalieri et al., 1996). Daily data were tabulated on a 25-km × 25-km Equal-Area Scalable Earth (EASE) grid across all points poleward of 60 N (Brodzik & Knowles, 2002). For each site and each day, the grid cell nearest to the site was determined by minimizing the great circle distance between the grid and the site location at noon. Average daily incident shortwave values were taken from the MERRA "Surface Incident Shortwave Flux Assuming a Clear Sky (SWGDNCLR)" array of the "tavg1_2d_rad_Nx" data subset. Ice concentrations were pulled for the corresponding grid cell each day.

The flux of solar heat input directly into the ocean through leads (F_{rL}) was calculated using

$$F_{rL} = F_r(1-\alpha_w)(1-\mathrm{C}) \tag{1}$$

where α_w is the albedo of open water (assumed as 0.07). The component of shortwave solar radiation incident on the ice was separated into components reflected to the atmosphere, absorbed in the ice, and transmitted to the ocean. The reflected light was computed using the ice-albedo as derived in Perovich et al. (2002) and Perovich, Jones et al. (2011), and it was assumed that all light not reflected was propagated into the ice. The average ice thickness for a grid cell (z) was obtained from the PIOMAS model (Zhang & Rothrock, 2003). The effective attenuation by the ice (K) was assigned a constant value 1.0 m^{-1} (Light et al., 2015, 2008). The flux of solar heat transmitted through the ice into the ocean was then computed using a Beer's Law approximation as follows:

$$F_{ri} = F_r(1-\alpha_i)(\mathrm{C})e^{(-Kz)} \tag{2}$$

The total flux into the ocean is the sum of F_{rL} and F_{ri}. These daily average fluxes with units of W m^{-2} can be transformed to daily heat input with units of MJ m^{-2} by simply multiplying by (86,400 s day^{-1})/(1,000,000 J MJ^{-1}).

Table 1
Tabulated Properties for the Eight Mass Balance Sites Studied

	1997A	2005B	2006C	2007E	2012L	2013F	2014C	2015J
Start date	10/25/1997	8/24/05	9/4/2006	8/16/2007	8/27/2012	8/25/2013	3/20/2014	9/28/2015
Start latitude	75.463	77.616	77.887	78.929	80.887	76.928	73.505	78.557
Start longitude	−143.563	−142.155	−140.399	−139.950	−137.923	−138.884	−137.340	−141.356
End date	9/22/1998	10/27/06	10/10/2007	8/22/2008	8/28/2013	6/26/2015	8/23/2014	10/7/2016
End latitude	80.297	74.839	76.868	74.745	73.986	77.293	74.505	77.223
End longitude	−166.237	−142.415	−143.150	−141.487	−145.646	−144.464	−156.090	−124.426
Initial ice thickness	187	328	286	304	334	139	182	169
Final ice thickness	145	305	108	65	234	107	82	102
Maximum snow depth	45	25	52	15	29	54	31	32
Maximum ice thickness	239.5	382	326	326	344	174	196	224
Total surface melt (s + i)	74.9	65.3	83.2	95.0	85.6	37.8	57.2	56.6
Total surface ice melt	60	57	66	90	76	20	47	46
Total bottom melt	43	77	215	220	103	61	107	113
Total ice growth	74	63	42	39	15	49	n/a	55
Net annual ice	−29	−71	−239	−271	−164	−32	n/a	−104
Surface snow melt onset	5/29/1998	6/10/2006	6/5/2007	5/16/2008	5/27/2013	6/12/2014	6/5/2014	6/2/2016
Surface ice melt onset	6/21/1998	6/29/2006	6/24/2007	5/20/2008	6/18/2013	7/7/2014	6/29/2014	6/12/2016
Bottom melt onset	6/5/1998	6/10/2006	6/5/2007	6/3/2008	6/3/2013	6/13/2014	6/1/2014	6/1/2016
Surface ice melt ending	8/17/1998	8/24/2006	8/30/2007	8/22/2008	8/12/2013	8/26/2014	8/22/2014	7/28/2016
Bottom melt ending	9/22/1998	10/14/2006	10/1/2007	Cont.	Cont.	9/21/2014	Cont.	Cont.
Freezing degree days	5,630	5,775	6,252	4,614	4,964	4,568	n/a	4,587

Note. All depth values are in cm. Entries of "Cont." indicate that melting continued, and entries of "n/a" mean that the data were unavailable. Dates are formatted as MM-DD-YYYY.

3. Results

The results from the eight sites are summarized in Table 1. Start and end dates and positions are reported, along with maximum snow depth and ice thickness, initial and final ice thickness, annual amounts of growth and melt, and onset dates of melt and freeze. Initial site latitude during deployment in the fall ranged from 75.5°N to 80.9°N and final summer latitudes from 74.0°N to 80.3°N. While the drift trajectories varied significantly from site to site, there was considerable overlap as the maps indicate (Figure 1). All sites were in the Beaufort Sea and spent most of their time over deep water.

The maximum ice thickness across the sites ranged from 174 to 382 cm, and maximum snow depths ranged from 15 to 54 cm. Ice growth varied by roughly a factor of 5 from 15 to 74 cm. Cumulative annual amounts of ice growth, surface melt, and bottom melt for the eight sites are presented in Figure 3 for comparison. The total amount of summer bottom melt ranged from 43 cm at site 1997A to 220 cm at 2007E. The smallest amount of bottom melt was for 1997A, followed by 2013F. On the surface, ice melt ranged from 20 cm in the summer of 2014 (2013F) to 90 cm in the summer of 2008 (2007E), with an average of 58 cm. Total surface melt was calculated as the combination of ice and ice-equivalent snow melt (S_i), defined as follows:

$$S_i = (\rho_s/\rho_i)\,\Delta S \tag{3}$$

where ρ_s is the density of snow (assumed to be 300 kg m^{-3}) and ρ_i the density of ice (assumed to be 900 kg m^{-3}) and ΔS is the thickness of snow melted. The lightly shaded area at the top of the surface melt bars in Figure 3 represents the ice-equivalent snow melt. Snow melt generally equated to 5 to 18 cm of ice-equivalent, and in all cases, the entire snow cover melted. Note that at all sites except 1997A, total amount of bottom melt amount exceeded surface melt. At the 2006C and 2007E sites, bottom melt was between 2.4 and 3.3 times greater than surface melt.

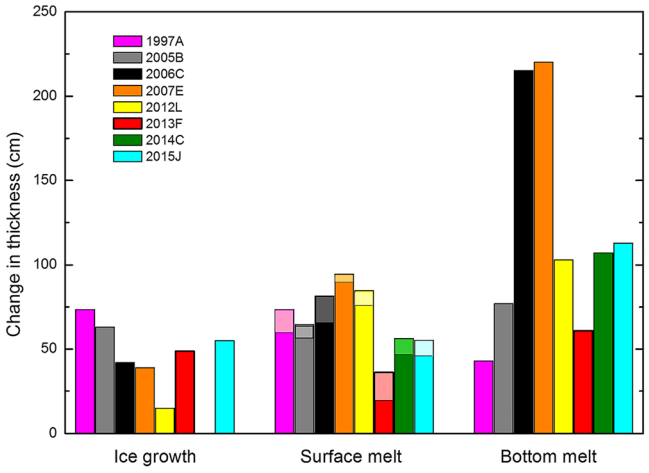

Figure 3. Total amounts of ice growth, surface ice, snow melt, and bottom melt. In the surface melt category, snow melt is converted to an ice equivalent volume and is denoted by the shaded area at the top of the bar.

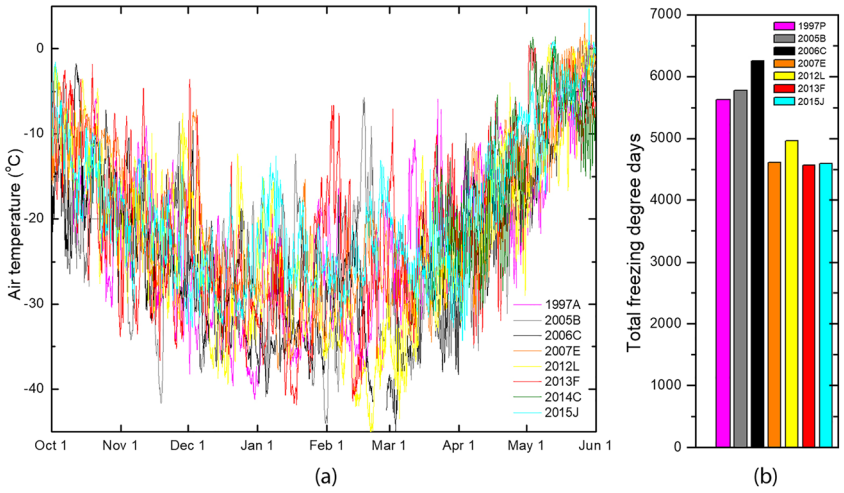

Figure 4. (a) Time series of air temperature for the eight sites from 1 September to 1 June. Considerable variation in daily temperature is found across years, with differences as large as 30° C on any given day. (b) Cumulative freezing degree days for the eight sites from 1 September to 1 June. Sites from 2007E onward all had significantly fewer freezing degree days, and the winters of sites 2007E, 2013F, and 2015J were all within 1% of each other.

Air temperatures measured at the sites from 1 September to 1 June are plotted in Figure 4a. On any given date, the air temperature varied greatly across sites and across years, with differences in winter typically around 20°C and as large as 30°C. As a measure of connection between air temperature and ice growth, the total number of freezing degree days (*FDD*) for seven sites (2014C was not installed until spring) was computed from 1 September to 1 June (Figure 4b). Freezing degree days are defined as the sum of the average daily temperature departure below 0°C, where the daily temperature is taken at the (S)IMB or in case of Site 1, SHEBA. Qualitatively, the number of freezing degree days is a cumulative measure of atmospheric forcing that can cause ice growth. Total freezing degree days ranged from a maximum of 6,252 days for the 2006–2007 winter (2006C) to a minimum of 4,568 days for the winter of 2013–2014 (2013F). The winters since 2006 all had substantially fewer freezing degree days. The freezing degree days for three of these winters, 2007–2008, 2013–2014, and 2015–2016, were within 1% of each other.

3.1. Growth and Melt Rates

The time series of surface melt (f_s) and ice growth and bottom melt (f_b) were determined on weekly intervals using the surface (P_s) and bottom (P_b) positions as follows:

$$f_s = (P_s\,(t+7) - P_s\,(t))/7 \tag{4}$$

$$f_b = -(P_b\,(t+7) - P_b\,(t))/7 \tag{5}$$

where t is a particular day and $t + 7$ is 7 days later. A coordinate system with zero located at the ice surface was used. Upward through the snow is negative, and downward to the ice is positive. Weekly averages are sufficient for measuring changes to ice surface and bottom position, which occur slowly. The weekly changes are divided by seven to give averaged daily rates. In this coordinate system, positive values of f indicate melt and negative values growth. There was no surface ice growth at any of the sites.

The daily rates of ice growth, surface melt, and bottom melt for the eight sites are plotted in Figure 5 along with ice thickness. Growth rates were generally greater at the thinner sites (1997A, 2013F, and 2015J) than the thicker sites (2006C, 2007E, and 2012L) and never exceeded 1 cm day^{-1}. An exception was 2005B, where the ice was more than 300 cm thick and winter growth rates were comparable to thin ice cases. This case had a thin snow cover and the second largest number of freezing degree days. In contrast, ice growth at site 2012L was sporadic and quite modest throughout the year, with a total growth of only 15 cm. The ice thickness at 2012L was greater than 300 cm throughout the fall and winter and had a maximum snow depth of 29 cm.

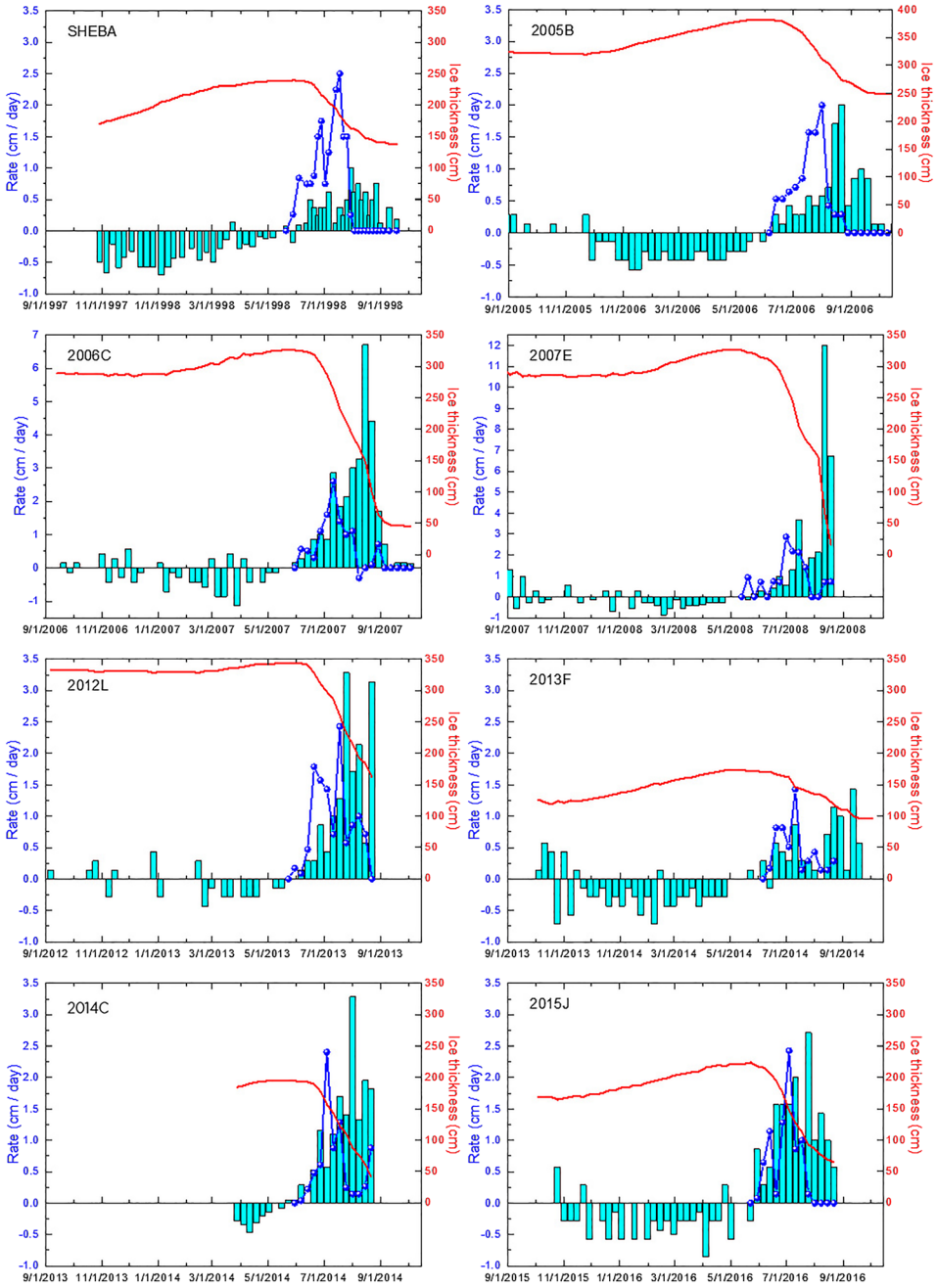

Figure 5. Time series of weekly averaged surface melt rate (blue line), ice growth rate, bottom melt rate (cyan bars), and ice thickness (red line). Negative rates are growth, positive are melt. Note that 2006C and 2007E have different vertical scales.

Peak surface melt rates were 2 to 2.5 cm day^{-1} for all sites except 2013F, where the peak surface melt rate was only 1.4 cm day^{-1}. In some cases, temporary halting of summer surface melt was observed, and in one case, summer snowfall was observed (2006C). This has also been observed in field experiments (Perovich, 2003; Perovich et al., 2017). Peak bottom melt rate for the eight sites ranged from 1 (1997A) to 12 cm day^{-1} (2007E) and always occurred after peak surface melt.

3.2. Mass Balance Event Timing

The events of interest in the cycle of sea ice mass balance are as follows: the onset dates of snow melt, surface ice melt, bottom ice melt, and the end dates of surface melt and bottom ice melt. The timing of mass balance

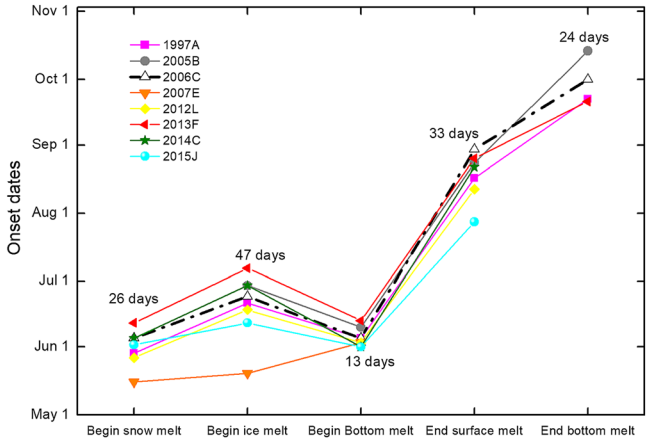

Figure 6. Date groupings and time spans of snow melt onset, surface ice melt onset, bottom melt onset, surface ice melt ending, and bottom melt ending. Note that four of the sites completely melted before the end of bottom melt. The number of days indicates the full time span for the onset/ending dates across all sites.

events, melt events in particular, is important as it plays a crucial role in determining the solar heat absorbed by the ocean (Stroeve et al., 2014). Mass balance event dates are plotted for each site in Figure 6 along with the date range for each of the events across sites. The onset date of snow melt was found to vary by almost a month from mid-May to mid-June, and the span of surface ice melt onset date is even greater at 47 days. In contrast, bottom melt onset occurred over a narrow window of 13 days from 1 June to 13 June and lasted up to 5 months in the case of 2006C. The end of surface melting varied widely from 28 July to 30 August but always ceased before bottom melting. All of the sites survived until the end of surface melting, but only four sites survived through bottom melting (1997A, 2005B, 2006C, and 2013F). For sites 2007E, 2012L, 2014C, and 2015J, the ice either completely melted or mechanically fell apart and then melted.

3.3. Solar Heat Input to Upper Ocean

The daily incident solar irradiance from April through October is plotted in Figure 7a. Large variations across sites and across days are observed, with differences of up to 200 W m^{-2} common. When time integrated over the April–September period, the total incoming solar heat varied between sites from 2,473 to 2,937 MJ m^{-2} and is likely due to the different latitudes of the sites during summer. The smallest total incoming solar heat was for site 1997A, which was the furthest north of the sites during summer. The largest was 2014C which was the furthest south in summer. It should be noted that the incident shortwave fluxes from the MERRA reanalysis product are only available up to 31 December 2014. Resultantly, the 2015J site was not included in this part of the analysis.

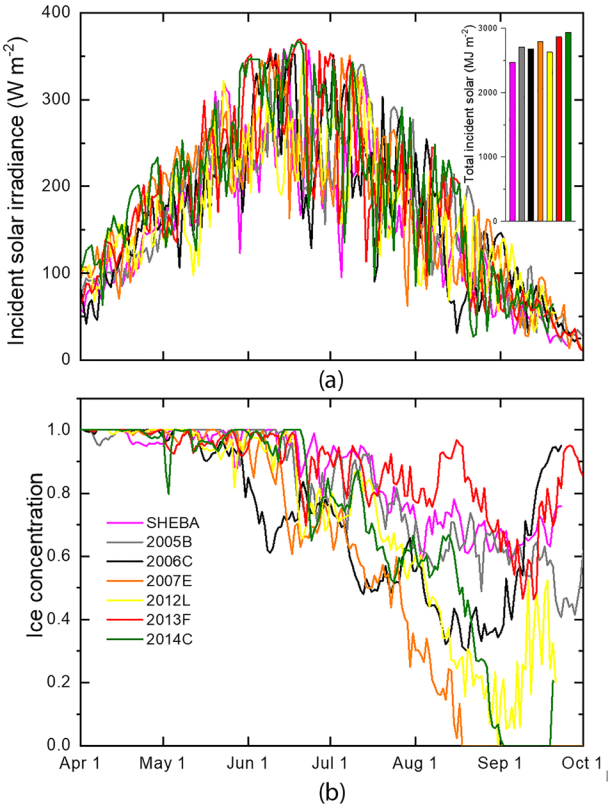

Figure 7. (a) Time series of daily incident solar irradiance from 1 April to 1 October for seven sites. The insert on the right shows the integrated incident solar heat during this period, with variations likely being due to latitude. (b) Time series of daily ice concentration at the 25-km grid cell nearest the site location at noon each day.

Ice concentrations taken daily at the grid cell nearest to each site at noon are plotted from 1 April to 1 October in Figure 7b. Ice concentrations are greater than 0.9 at all sites until early June when different trajectories emerge. For example, 2006C dips to an ice concentration of only 0.6 in early June, while all other sites remain greater than 0.8. As summer progresses, the variation in ice concentration between sites increases, reaching a peak in mid-August to September when ice concentrations range from zero to nearly one. Three of the sites reached zero concentration by the end of summer (2007E, 2012L, and 2014C).

From the time series of incident solar irradiance and ice concentrations, the estimated cumulative monthly solar heat input to the upper ocean for seven of the sites was computed and plotted from May to September in Figure 8. The monthly values are the sum of the daily heat input at the 25-km grid cell nearest the site trajectory each month. The heat input is broken down into two components: solar energy deposited through leads and solar energy transmitted through the ice. Very little heat is deposited into the ocean prior to May, and of the heat deposited, the majority was transmitted through the ice since there is very little open water during this period. From June–September, solar heat deposition through leads was the largest contributor to upper ocean heat. One site (2013F) had roughly equal monthly contributions from leads and from transmission through the ice during this time period. 2013F had the largest summer ice concentrations of all the sites and the second smallest solar heat input to the ocean.

Figures 9a–9h show the regional ice concentration map near the site on 15 August with the site location at noon indicated by the colored dot. The 15 August was chosen because it was near the time of maximum bottom melt rate at all sites. The colored bars in the lower right-hand corner of each

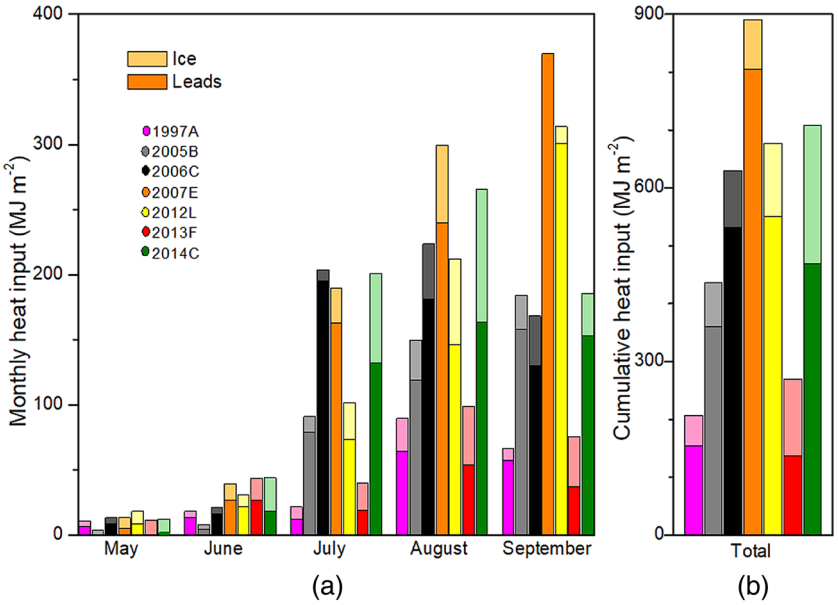

Figure 8. (a) Monthly solar heat input to the upper ocean from May through September. (b) The cumulative solar heat input. Contributions from leads are on the bottom (darker colors), and transmission through the ice is the shaded bar on the top (lighter colors). These values were computed using MERRA incident shortwave solar fluxes and passive microwave ice concentration values along the site drift track.

plot denote the relative amounts of bottom melting experienced over the 1 April to 1 October period. There is a statistically significant correlation ($R^2 = 0.69$, $p < 0.001$) between average ice concentration along the site trajectory from 1 April to 1 October and the amount of observed bottom melting (Figure 9i). Regional ice concentration and site proximity to the ice edge during summer are also noticeable as contributing factors to bottom melt. For instance, sites 2007E, 2012L, and 2015J were right near the ice edge and experienced the first, third, and fourth largest amounts of bottom melting, respectively. The site with the second largest amount of bottom melt (2006C) was inward from the ice edge but in an area of very low concentration. A commonality among the sites with the lowest amounts of bottom melting was an inward location from the ice edge and a more homogenous surrounding of higher concentration ice.

3.4. Correlations Between Mass Balance Parameters

Relationships between quantities are compared in Figure 10 with the goal of identifying potential mass balance proxies. In all subplots, a 5% confidence interval was used to declare statistical significance. On the surface, there was a modest and statistically significant relationship (Figure 10a, $R^2 = 0.57$, $p = 0.0135$) between the start of melt and the total amount of surface melt. This result corroborates the trend of earlier melt onset amplifying ice loss across the Arctic, especially in the Beaufort (Stroeve et al., 2014). The most significant relationship was observed between the maximum snow depth and the start date of surface ice melt, with larger snow depths corresponding to later start dates of ice melt (Figure 10b, $R^2 = 0.61$, $p = 0.014$). This is simply because all snow must melt before ice surface melt can begin. The remaining subplots of Figures 10c–10i were not statistically significant at a 5% confidence interval. These comparisons demonstrate that simple, one-dimensional, proxies for mass balance are difficult to establish.

3.5. Heat Used in Melting Versus Solar Heat Deposited Into the Ice and Ocean

Heat used for surface and bottom melting are compared to the heat available for melting in Figure 11. For the surface, the heat used for melting is determined as follows:

$$Q_{ms} = \rho_s L_f \Delta H_s + \rho_i L_f \Delta H_i \tag{6}$$

where ρ_s is the average density of Arctic snow (300 kg m^{-3}), ρ_i is the average density of sea ice (900 kg m^{-3}), L_f is the average latent heat of fusion of sea ice (334 kJ kg^{-1}), ΔH_s is the amount of snow melt, and ΔH_i is the

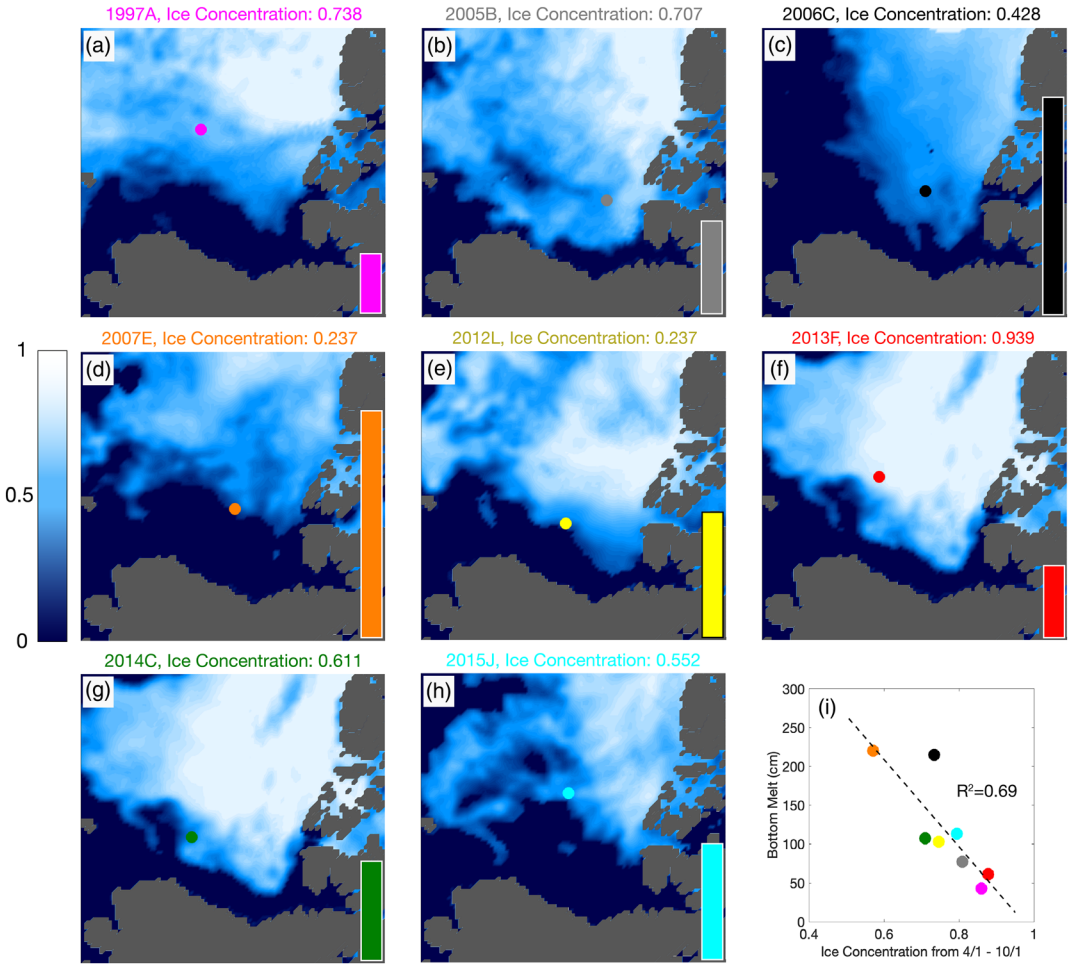

Figure 9. (a–h) Regional ice concentration maps and position on 15 August of the relevant year for the eight sites. The bar in the lower right-hand corner represents the relative amounts of bottom melting observed at the site over the 1 April to 10 October time span. (i) A scattergram showing cumulative bottom melt versus average ice concentration along each site trajectory from 1 April to 1 October ($p < 0.001$).

amount of surface ice melt. The heat available for surface melting was the time-integrated solar flux to the ice from spring sunrise through the end of surface melt and was computed using MERRA incident shortwave solar values and satellite-derived ice concentrations (as described in section 2.2). This heat can also be visualized as the summation of the shaded subsections atop each bar in Figure 8. No statistically significant correlation (Figure 11a) was found between heat available for surface melting and the heat used for surface melting; however, in all cases ample heat was provided for the observed melt (all points lie above the 1/1 line). In the case of 2014C, this excess was over 4 times the heat used in surface melting. It is likely that this overestimate of available heat is a result of several factors, most notably being uncertainties in the MERRA-derived incident shortwave values and spring and summertime albedo evolution.

On the bottom surface, the heat used in melting, Q_{mb} is given by

$$Q_{mb} = \rho_i \, L_f \, \Sigma \, (\Delta H_b(t) \, C(t)) \tag{7}$$

where ΔH_b and C are the time series of bottom ice melt and the ice concentration at the site position, respectively. The heat available for bottom melting was taken to be the cumulative (1 April to 1 October) heat input to the grid cell nearest the site on 15 August and was chosen because 15 August is around the time of peak bottom melt rate at all sites. The component of solar heat transmitted through the ice into the ocean was

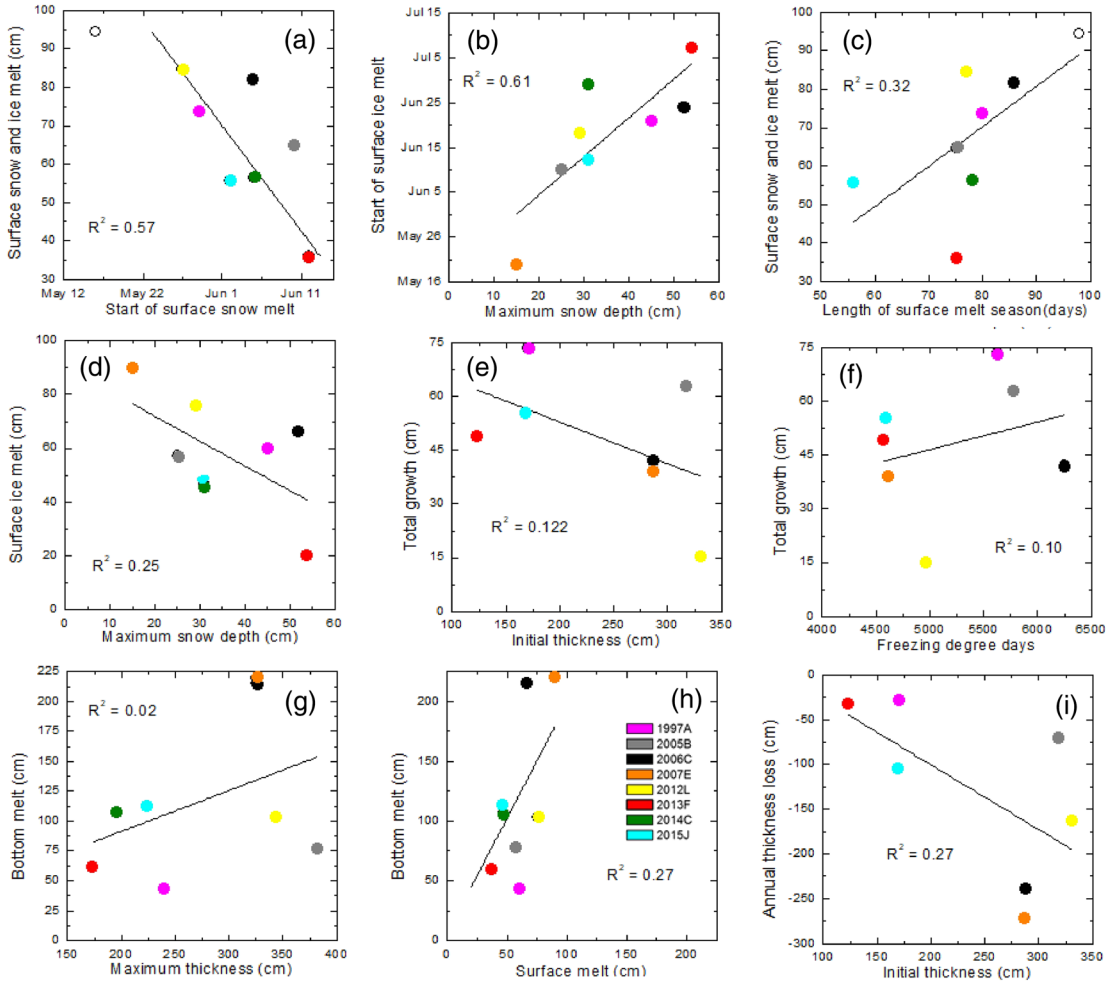

Figure 10. (a–i) Scattergrams examining relationships between different mass balance parameters. Note that while some comparisons are statistically significant, many of the plots show large scatter. Of these relationships, only plots (e) and (g) are statistically significant at the 5% confidence interval.

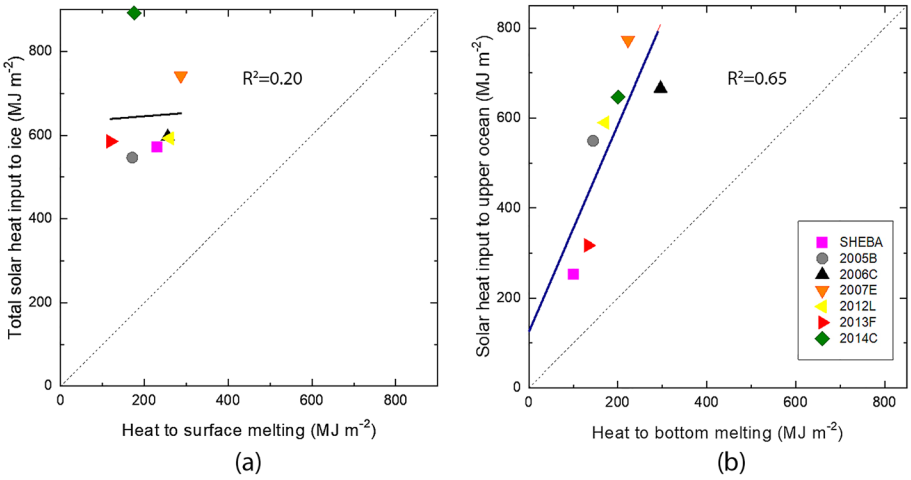

Figure 11. (a) Heat used for surface melting versus the total solar heat input to the ice. (b) Heat used for bottom melting versus the total solar heat input to the upper ocean from leads and transmission through the ice. The 1/1 dashed line represents where heat used in melting equals solar heat input. Points above and to the left mean that there is an ample supply of solar heat. The solid blue line is the linear least squares fit.

computed by the same method as presented in section 2.2 and Figure 8. A statistically significant relationship between heat used in bottom melting and heat available for bottom melting was found ($R^2 = 0.65$, $p = 0.031$). There was also significantly more heat deposited into the ocean than what was used in bottom melting, with excesses ranging from around 50 MJ m^{-2} at 1997A to over 500 MJ m^{-2} at 2007E.

4. Summary and Discussion

In this work, time series observations from eight sea ice mass balance sites in the Beaufort Sea spanning 1997–2015 were analyzed. At each site, the time series of sea ice surface and bottom position were determined through an annual growth and melt cycle (with exception of 2014C, which was installed after the growth cycle). The time series of ice growth and surface and bottom melting were then compared to estimates of atmospheric and ocean heat fluxes along the site drift track. Over the 18-year span from 1997 to 2015, all of the sites studied showed an annual net loss of ice between 29 and 271 cm. Seven of the eight sites, all of which were in the 21st century, showed more bottom melt than surface melt, and observed bottom melt was correlated to average ice concentration along the trajectory. Likewise, an equally strong correlation between the amount of bottom melt and the solar heat deposited into the ocean nearest the site location (25-km grid cell) on 15 August of the respective year was also found. Interestingly, despite large differences in site trajectory (Figure 1), summer latitude (Table 1), and spring ice concentration (Figure 7b), bottom melt initiated within a narrow 13-day window between 1 June and 13 June at all sites. Between observed quantities, statistically significant correlations were found between surface (snow + ice) melt and snow melt onset date and surface ice melt onset and maximum snow depth.

4.1. Relationship Between Upper Ocean Solar Heat Input and Ice Loss

Sea ice mass balance is controlled by a complex interplay of dynamic and thermodynamic processes. In the summer, the primary driving force of ice melt is the ice-albedo feedback, caused by ice melting and exposing open water or creating melt ponds, which in turn absorb more solar energy and melt more ice. The solar heat absorbed through leads is a significant contributor to the ice-albedo feedback, which has increased across the Arctic as ice concentrations decrease and melt seasons lengthen (Kashiwase et al., 2017; D. K. Perovich et al., 2011). This trend has been especially pronounced in the Beaufort, where heat excesses from May–September can be enough to melt 0.97–1.3 m of ice during summer (Stroeve et al., 2014). Results from this study show a direct connection between heat absorption in the upper ocean and observed amounts of bottom melt. At all but one site (1997A), the majority of ice loss was from bottom melting, and all cases had excess solar heat for the observed amount of melt. This excess heat can amplify sea ice melt in the present, and also precondition the ocean, limiting (or preventing) ice growth the following fall (Babb et al., 2016; Perovich et al., 2008). This has culminated in a decrease in mean ice thickness as a trend and also as periodic large reductions in sea ice as a result of summer heat absorption anomalies (Babb et al., 2016; Perovich et al., 2008). The connection between ocean solar heat input and bottom melt indicates that projected decreases in yearly mean ice concentration in the Beaufort will continue to drive ice loss.

4.2. Melt Onset Timing and Magnitude

Solar heat anomalies and corresponding ice loss are highly sensitive to the timing of melt onset (Stroeve et al., 2014). The earlier leads and melt ponds are formed; the more sunlight they will absorb, and the more melting they will cause. The amount of surface (in this case, snow + ice) melt was correlated to the onset date of snow melt, with earlier onset dates leading to increased surface melt. Total surface melt was not correlated to the total length of the melt season, however. Both of these findings are in line with results from the SHEBA campaign, which found melt onset to exert much more control over cumulative melt than freezing onset (Perovich et al., 2007). On the bottom, melt onset across the window from 1–13 June is interesting. In particular, the narrow 13-day clustering is tighter than all other onset/ending events and generally occurred before large reductions in ice concentration and resultant increases in upper ocean solar heat deposition. One possible explanation for the narrow window of melt onset would be an Arctic-scale, seasonal heat flux, such as warm water advection through the Bering Strait that has been shown to trigger bottom melt on a regional scale (Woodgate et al., 2010). However, these fluxes exhibit large seasonal and interannual variability (Woodgate et al., 2012). Another explanation would be to examine the basal energy budget, which is balanced by the ocean heat flux and conduction through the ice (Untersteiner, 1961). In comparison to the surface energy budget, which is highly sensitive to interannual variabilities in air temperature and

radiative fluxes, the basal energy balance responds more slowly. Thus, variations in atmospheric forcing are dampened and bottom melt initiation occurs more predictably.

4.3. Uncertainties and Future Observational Campaigns

While the findings in this work demonstrate and corroborate several compelling trends, spatial and temporal variability remains high on seasonal and interannual timescales. Because (S)IMB results represent point measurements, it is clear that a more convincing story can always be told with a more extensive data set. Continued support of observational campaigns is thus paramount to the ground truth understanding of the changes occurring to Arctic sea ice and the forcings that caused them. In particular, future observational programs would ideally focus on increasing instrument quantity to sample mass balance more frequently in space, thus giving multiple data points for a given year to greatly improve statistical quantification. Field campaigns such as the Multidisciplinary drifting Observatory for the Study of Arctic Climate (MOSAiC) are also extremely promising and will hopefully contribute valuable understanding of the driving forces behind past, present, and future changes to Arctic sea ice.

Data Availability Statement

The IMB and SIMB data used in this manuscript are archived and publicly available online (http://imb-crrel-dartmouth.org/archived-data/).

Acknowledgments

The authors are grateful to the Beaufort Gyre Exploration Project and the Woods Hole Oceanographic Institute for their excellent support in deploying and maintaining the Ice Mass Balance Buoy network. Special thanks to J. A. Richter-Menge, C. M. Polashenski, B. Elder, J. Parno, G. Passow, and K. Jones for their many helpful discussions in preparing this manuscript. This work has been supported by the National Science Foundation (Grant 1560908) and the National Oceanic and Atmospheric Administration.

References

Babb, D. G., Galley, R. J., Barber, D. G., & Rysgaard, S. (2016). Physical processes contributing to an ice free Beaufort Sea during September 2012. *Journal of Geophysical Research: Oceans*, *121*, 267–283. https://doi.org/10.1002/2015JC010756

Brodzik, M. J., & Knowles, K. W. (2002). Chapter 5: EASE-grid: A versatile set of equal-area projections and grids, in: Discrete Global Grids: A Web Book.

Carmack, E., & Melling, H. (2011). Cryosphere: Warmth from the deep. *Nature Geoscience*, *4*, 7–8. https://doi.org/10.1038/ngeo1044

Cavalieri, D. J., Parkinson, C. L., Gloersen, P., & Zwally, H. J. (1996). Sea ice concentrations from Nimbus-7 SMMR and DMSP SSM/I-SSMIS passive microwave data, Version 1. https://doi.org/10.5067/8GQ8LZQVL0VL

Comiso, J. C. (2012). Large decadal decline of the arctic multiyear ice cover. *Journal of Climate*, *25*(4), 1176–1193. https://doi.org/10.1175/JCLI-D-11-00113.1

Haas, C., Goff, H. L. E., Audrain, S., Perovich, D., & Haapala, J. (2011). Comparison of seasonal sea-ice thickness change in the transpolar drift observed by local ice mass-balance observations and floe-scale EM surveys. *Annals of Glaciology*, *52*(57), 97–102. https://doi.org/10.3189/172756411795931778

Holland, M. M., Bitz, C. M., & Tremblay, B. (2006). Future abrupt reductions in the summer Arctic sea ice. *Geophysical Research Letters*, *33*, L23503. https://doi.org/10.1029/2006GL028024

Hutchings, J. K., & Perovich, D. K. (2015). Preconditioning of the 2007 sea-ice melt in the eastern Beaufort Sea, Arctic Ocean. *Annals of Glaciology*, *56*(69), 94–98. https://doi.org/10.3189/2015AoG69A006

Hutchings, J. K., & Rigor, I. G. (2012). Role of ice dynamics in anomalous ice conditions in the Beaufort Sea during 2006 and 2007. *Journal of Geophysical Research*, *117*, C00E04. https://doi.org/10.1029/2011JC007182

Jackson, K., Wilkinson, J., Maksym, T., Meldrum, D., Beckers, J., Haas, C., & Mackenzie, D. (2013). A novel and low-cost sea ice mass balance buoy. *Journal of Atmospheric and Oceanic Technology*, *30*, 2676–2688. https://doi.org/10.1175/JTECH-D-13-00058.1

Kashiwase, H., Ohshima, K. I., Nihashi, S., & Eicken, H. (2017). Evidence for ice-ocean albedo feedback in the Arctic Ocean shifting to a seasonal ice zone. *Scientific Reports*, *7*(1), 8170. https://doi.org/10.1038/s41598-017-08467-z

Kay, J. E., & Gettelman, A. (2009). Cloud influence on and response to seasonal Arctic sea ice loss. *Journal of Geophysical Research*, *114*, D18204. https://doi.org/10.1029/2009JD011773

King, J., Spreen, G., Gerland, S., Haas, C., Hendricks, S., Kaleschke, L., & Wang, C. (2017). Sea-ice thickness from field measurements in the northwestern Barents Sea. *Journal of Geophysical Research: Oceans*, *1*, 1497–1512. https://doi.org/10.1002/2016JC012199.Received

Krishfield, R., Proshutinsky, A., Tateyama, K., Williams, W., Carmack, E. C., & Timmermans, M.-L. (2014). Journal of geophysical research: Oceans. *Journal of Geophysical Research: Oceans*, *119*, 1271–1305. https://doi.org/10.1002/2013JC008999

Kwok, R., & Cunningham, G. F. (2010). Contribution of melt in the Beaufort Sea to the decline in Arctic multiyear sea ice coverage: 1993–2009. *Geophysical Research Letters*, *37*, L20501. https://doi.org/10.1029/2010GL044678

Kwok, R., Cunningham, G. F., Wensnahan, M., Rigor, I., Zwally, H. J., & Yi, D. (2009). Thinning and volume loss of the Arctic Ocean sea ice cover: 2003-2008. *Journal of Geophysical Research*, *114*, C07005. https://doi.org/10.1029/2009JC005312

Kwok, R., & Rothrock, D. A. (2009). Decline in Arctic sea ice thickness from submarine and ICESat records: 1958–2008. *Geophysical Research Letters*, *36*, L15501. https://doi.org/10.1029/2009GL039035

Lange, B. A., Flores, H., Michel, C., Beckers, J. F., Castellani, G., Hatam, I., et al. (2017). Pan-Arctic sea ice-algal chl a biomass and suitable habitat are largely underestimated for multiyear ice 4581–4597. *Global Change Biology*, *23*, 4581–4597. https://doi.org/10.1111/gcb.13742

Lei, R., Cheng, B., Heil, P., Vihma, T., Wang, J., Ji, Q., & Zhang, Z. (2018). Seasonal and interannual variations of sea ice mass balance from the central Arctic to the Greenland Sea. *Journal of Geophysical Research: Oceans*, *123*, 2422–2439. https://doi.org/10.1002/2017JC013548

Light, B., Grenfell, T. C., & Perovich, D. K. (2008). Transmission and absorption of solar radiation by Arctic sea ice during the melt season. *Journal of Geophysical Research*, *113*, C03023. https://doi.org/10.1029/2006JC003977

Light, B., Perovich, D. K., Webster, M. A., Polashenski, C. M., & Dadic, R. (2015). Optical properties of melting first-year Arctic sea ice. *Journal of Geophysical Research: Oceans*, *120*, 7657–7675. https://doi.org/10.1002/2015JC011163.Received

Lindsay, R. W., Zhang, J., Schweiger, A., Steele, M., & Stern, H. (2009). Arctic sea ice retreat in 2007 follows thinning trend. *Journal of Climate*, *22*(1), 165–176. https://doi.org/10.1175/2008JCLI2521.1

Maslanik, J., Stroeve, J., Fowler, C., & Emery, W. (2011). Distribution and trends in Arctic sea ice age through spring 2011. *Geophysical Research Letters*, *38*, L13502. https://doi.org/10.1029/2011GL047735

Overland, J. E., & Wang, M. (2005). The third Arctic climate pattern: 1930s and early 2000s. *Geophysical Research Letters*, *32*, L23808. https://doi.org/10.1029/2005GL024254

Perovich, D., Polashenski, C., Arntsen, A., & Stwertka, C. (2017). Anatomy of a late spring snowfall on sea ice. *Geophysical Research Letters*, *44*, 2802–2809. https://doi.org/10.1002/2016GL071470

Perovich, D., & Richter-Menge, J. A. (2006). From points to Poles: extrapolating point measurements of sea-ice mass balance. *Annals of Glaciology*, *44*, 188–192. https://doi.org/10.3189/172756406781811204

Perovich, D. K. (2003). Thin and thinner: Sea ice mass balance measurements during SHEBA. *Journal of Geophysical Research*, *108*(C3), 8050. https://doi.org/10.1029/2001JC001079

Perovich, D. K., & Elder, B. (2002). Estimates of ocean heat flux at SHEBA. *Geophysical Research Letters*, *29*(9), 1344. https://doi.org/10.1029/2001GL014171

Perovich, D. K., Grenfell, T. C., & Hobbs, P. V. (2002). Seasonal evolution of the albedo of multiyear Arctic sea ice. *Journal of Geophysical Research*, *107*(C10), 8044. https://doi.org/10.1029/2000JC000438

Perovich, D. K., Jones, K. F., Light, B., Eicken, H., Markus, T., Stroeve, J., & Lindsay, R. (2011). Solar partitioning in a changing Arctic sea-ice cover. *Annals of Glaciology*, *52*(57), 192–196. https://doi.org/10.3189/172756411795931543

Perovich, D. K., Nghiem, S. V., Markus, T., & Schweiger, A. (2007). Seasonal evolution and interannual variability of the local solar energy absorbed by the Arctic sea ice—Ocean system. *Journal of Geophysical Research*, *112*, C03005. https://doi.org/10.1029/2006JC003558

Perovich, D. K., Richeter-Menge, J. A., Jones, K. F., & Light, B. (2008). Sunlight, water, and ice: Extreme Arctic sea ice melt during the summer of 2007. *Geophysical Research Letters*, *35*, L11501. https://doi.org/10.1029/2008GL034007

Perovich, D. K., & Richter-Menge, J. A. (2015). Regional variability in sea ice melt in a changing Arctic. *Philosophical Transactions. Series A, Mathematical, Physical, and Engineering Sciences*, *373*, 20140165. https://doi.org/10.1098/rsta.2014.0165

Perovich, D. K., Richter-Menge, J. A., Jones, K. F., Light, B., Elder, B. C., Polashenski, C., et al. (2011). Arctic sea-ice melt in 2008 and the role of solar heating. *Annals of Glaciology*, *52*(57), 355–359. https://doi.org/10.3189/172756411795931714

Perovich, D., Richter-Menge, J., Polashenski, C., Elder, B., Arbetter, T., & Brennick, O. (2014). Sea ice mass balance observations from the North Pole Environmental Observatory. *Geophysical Research Letters*, *41*, 2019–2025. https://doi.org/10.1002/2014GL059356

Petty, A., Hutchings, J. K., Richter-Menge, J. A., & Tschudi, M. A. (2016). Sea ice circulation around the Beaufort Gyre: The changing role of wind forcing and the sea ice state. *Journal of Geophysical Research: Oceans*, *121*, 3278–3296. https://doi.org/10.1002/2015JC011486. Received

Planck, C. J., Whitlock, J., Polashenski, C., & Perovich, D. (2019). The evolution of the seasonal ice mass balance buoy. *Cold Regions Science and Technology*, *165*, 102792. https://doi.org/10.1016/j.coldregions.2019.102792

Polashenski, C., Perovich, D., Richter-Menge, J., & Elder, B. (2011). Seasonal ice mass-balance buoys: Adapting tools to the changing Arctic. *Annals of Glaciology*, *52*(57), 18–26. https://doi.org/10.3189/172756411795931516

Richter-Menge, J. A., Perovich, D. K., Elder, B. C., Claffey, K., Rigor, I., & Ortmeyer, M. (2006). Ice mass balance buoys: A tool for measuring and attributing changes in the thickness of the Arctic sea ice cover. *Annals of Glaciology*, *44*, 205–210. https://doi.org/10.3189/172756406781811727

Rienecker, M. M., Suarez, M. J., Gelaro, R., Todling, R., Bacmeister, J., Liu, E., et al. (2011). MERRA: NASA's modern-era retrospective analysis for research and applications. *Journal of Climate*, *24*(14), 3624–3648. https://doi.org/10.1175/JCLI-D-11-00015.1

Serreze, M. C., Barrett, A. P., Stroeve, J. C., Kindig, D. N., & Holland, M. M. (2009). The cryosphere the emergence of surface-based Arctic amplification. *The Cryosphere*, *3*, 11–19. https://doi.org/10.5194/tc-3-11-2009

Serreze, M. C., & Meier, W. N. (2019). The Arctic' s sea ice cover: Trends, variability, predictability, and comparisons to the Antarctic. *Annals of the New York Academy of Sciences*, *1436*, 36–53. https://doi.org/10.1111/nyas.13856

Stroeve, J. C., Kattsov, V., Barrett, A., Serreze, M., Pavlova, T., Holland, M., & Meier, W. N. (2012). Trends in Arctic sea ice extent from CMIP5, CMIP3 and observations. *Geophysical Research Letters*, *39*, L16502. https://doi.org/10.1029/2012GL052676

Stroeve, J. C., Markus, T., Boisvert, L., Miller, J., & Barret, A. (2014). Geophysical changes in Arctic melt season and implications for sea ice loss letters. *Geophysical Research Letters*, *41*, 1216–1225. https://doi.org/10.1002/2013GL058951.Received

Thorndike, A. S., & Colony, R. (1982). Sea ice motion in response to geostrophic winds. *Journal of Geophysical Research*, *87*(C8), 5845. https://doi.org/10.1029/jc087ic08p05845

Untersteiner, N. (1961). On the mass and heat budget of Arctic sea ice. *Archiv für Meteorologie, Geophysik und Bioklimatologie Serie A*, *12*(2), 151–182. https://doi.org/10.1007/BF02247491

Wang, L., Derksen, C., Brown, R., & Markus, T. (2013). Recent changes in pan-Arctic melt onset from satellite passive microwave measurements. *Geophysical Research Letters*, *40*, 522–528. https://doi.org/10.1002/grl.50098

Woodgate, R. A., Weingartner, T., & Lindsay, R. (2010). The 2007 Bering Strait oceanic heat flux and anomalous Arctic sea-ice retreat. *Geophysical Research Letters*, *37*, L01602. https://doi.org/10.1029/2009GL041621

Woodgate, R. A., Weingartner, T. J., & Lindsay, R. (2012). Observed increases in Bering Strait oceanic fluxes from the Pacific to the Arctic from 2001 to 2011 and their impacts on the Arctic Ocean water column. *Geophysical Research Letters*, *39*, L24603. https://doi.org/10.1029/2012GL054092

Zhang, J., & Rothrock, D. A. (2003). Modeling global sea ice with a thickness and enthalpy distribution model in generalized curvilinear coordinates. *Monthly Weather Review*, *131*(5), 845–861. https://doi.org/10.1175/1520-0493(2003)131<0845:MGSIWA>2.0.CO;2